

# Structural determinants for regulation of phosphodiesterase by a G protein at 2.0 Å

Kevin C. Slep\*†‡, Michele A. Kercher\*‡§, Wei He||, Christopher W. Cowan†||, Theodore G. Wensell|| & Paul B. Sigler\*§

\* Department of Molecular Biophysics and Biochemistry, and § Howard Hughes Medical Institute, Yale University, New Haven, Connecticut 06511, USA

|| Verna and Marrs McLean Department of Biochemistry and Molecular Biology, Baylor College of Medicine, Houston, Texas 77030, USA

‡ These authors contributed equally to this work

† Present addresses: Department of Cellular and Molecular Pharmacology and Howard Hughes Medical Institute, University of California, San Francisco, California 94143, USA (K.C.S.); Division of Neuroscience, Children's Hospital, and Department of Neurobiology, Harvard Medical School, Boston, Massachusetts 02115, USA (C.W.C.)

A multitude of heptahelical receptors use heterotrimeric G proteins to transduce signals to specific effector target molecules. The G protein transducin,  $G_t$ , couples photon-activated rhodopsin with the effector cyclic GMP phosphodiesterase (PDE) in the vertebrate phototransduction cascade. The interactions of the  $G_t$   $\alpha$ -subunit ( $\alpha_t$ ) with the inhibitory PDE  $\gamma$ -subunit (PDE $\gamma$ ) are central to effector activation, and also enhance visual recovery in cooperation with the GTPase-activating protein regulator of G-protein signalling (RGS)-9 (refs 1–3). Here we describe the crystal structure at 2.0 Å of rod transducin  $\alpha$ -GDP·AlF $_4^-$  in complex with the effector molecule PDE $\gamma$  and the GTPase-activating protein RGS9. In addition, we present the independently solved crystal structures of the RGS9 RGS domain both alone and in complex with  $\alpha_{t/i1}$ -GDP·AlF $_4^-$ . These structures reveal insights into effector activation, synergistic GTPase acceleration, RGS9 specificity and RGS activity. Effector binding to a nucleotide-dependent site on  $\alpha_t$  sequesters PDE $\gamma$  residues implicated in PDE inhibition, and potentiates recruitment of RGS9 for hydrolytic transition state stabilization and concomitant signal termination.

Crystals were obtained using the RGS9 RGS domain (residues 276–422), an NΔ25 $\alpha_{t/i1}$  chimaera, and PDE $\gamma$  (residues 46–87). The NΔ25 $\alpha_{t/i1}$  chimaera is identical to  $\alpha_t$  except for residues 216–294 which are replaced with the corresponding homologous region of

$\alpha_{i1}$  (residues 220–298)<sup>4</sup>. The  $\alpha_{t/i1}$  chimaera interacts with PDE $\gamma_{46-87}$  and displays an augmented rate of RGS9<sub>276-422</sub>/PDE $\gamma_{46-87}$ -mediated GTP hydrolysis<sup>5</sup> (data not shown). The constructs that we used reflect functional recombinant components that yield diffraction-quality crystals. All three structures were solved by multiwavelength anomalous dispersion (MAD) phasing using selenomethionine (Se-Met)-substituted RGS9. Diffraction data and final refinement statistics are presented in Table 1.

The structure of the  $\alpha_{t/i1}$ -GDP·AlF $_4^-$ -PDE $\gamma$ -RGS9 complex is depicted in Fig. 1. Secondary structure observed in the heterotrimeric complex is diagrammed in Fig. 2. The  $\alpha_{t/i1}$  subunit is composed of two domains: a Ras-like GTPase and an  $\alpha$ -helical domain. Previous structural studies<sup>6,7</sup> identified three switch regions (I–III) in  $\alpha_t$  that undergo nucleotide-dependent conformational changes (Fig. 2). The overall structure of the  $\alpha_{t/i1}$  subunit and its switch region architecture most closely resembles the transition state analogue structure  $\alpha_t$ -GDP·AlF $_4^-$  (ref. 8). The RGS9 RGS domain is structurally homologous to the RGS domains of RGS4 (ref. 9), axin<sup>10</sup> and G alpha interacting protein (GAIP)<sup>11</sup>. Nine helices are configured into two subdomains: an amino- and carboxy-terminal region (helices  $\alpha_1$ ,  $\alpha_2$ ,  $\alpha_3$ ,  $\alpha_8$  and  $\alpha_9$ ), and a prototypical right-handed, antiparallel four-helix bundle (helices  $\alpha_4$ ,  $\alpha_5$ ,  $\alpha_6$  and  $\alpha_7$ ). The two subdomains are united by a hydrophobic interface. All independently refined structures of the RGS9 RGS domain show similar secondary structure with minor variations in helix length and in the occurrence of single turn helices in loops not used in  $G_\alpha$  binding. PDE $\gamma_{46-87}$  comprises three short  $\alpha$ -helices and an N-terminal loop region that originates near the C terminus and winds over helices  $\alpha_1$  and  $\alpha_2$ . Helices  $\alpha_1$  and  $\alpha_2$  adopt a relative orientation that presents the critical residue of PDE $\gamma$ , Trp 70, to  $\alpha_{t/i1}$ .

PDE $\gamma$  engages the  $\alpha_{t/i1}$  switch II/ $\alpha_3$  cleft in a hydrophobic interlock that buries 1,500 Å<sup>2</sup> of solvent-accessible surface (Fig. 3a–f). Interactions are shown in Fig. 3b. Whereas binding involves primarily hydrophobic interactions with an electrostatically neutral region of  $\alpha_{t/i1}$ , the PDE $\gamma$  interface has a relatively negative charge distribution (Fig. 4). Trp 70 of PDE $\gamma$  has a key role in the  $\alpha_{t/i1}$  interaction. Transgenic and *in vitro* studies using the PDE $\gamma$  mutant Trp70Ala confirm the role of Trp 70 in  $\alpha_{t/i1}$  binding and GTPase-activating protein (GAP) potentiation<sup>12,13</sup> (Fig. 3b). The Trp70Ala mutation slows the flash response recovery rate, decreases affinity for  $\alpha_t$  fivefold, and fails to augment GAP activity. In the  $\alpha_{t/i1}$ -GDP·AlF $_4^-$ -PDE $\gamma$ -RGS9 structure, Trp 70 binds the switch II/ $\alpha_3$  cleft, forming hydrophobic contacts with seven residues from

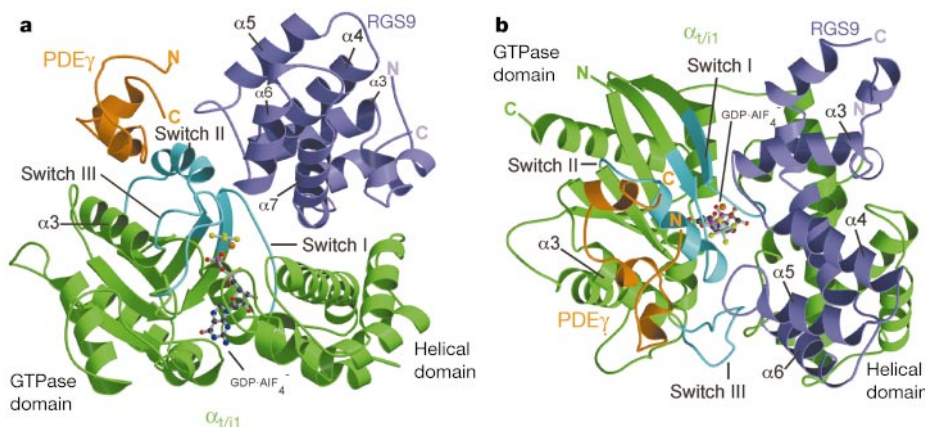


**Figure 1** Structure of the  $\alpha_{t/i1}$ -GDP·AlF $_4^-$ -PDE $\gamma$ -RGS9 heterotrimeric complex with  $\alpha_{t/i1}$  shown in green, the switch regions of  $\alpha_{t/i1}$  shown in blue, PDE $\gamma$  shown in orange and RGS9 shown in lavender. **a**, Ribbon drawing of the heterotrimeric complex with GDP and AlF $_4^-$  shown as ball-and-stick models. Carbon, nitrogen, oxygen, phosphorus, fluoride and

aluminium atoms are coloured black, blue, red, magenta, yellow-green and green, respectively. Mg<sup>2+</sup> is represented by an orange sphere. **b**, Ribbon drawing of the complex as in **a**, rotated 90° about the horizontal axis.

switch II and  $\alpha 3$  (Fig. 3b, 3d). A hydrogen bond between Ser 248 of  $\alpha_{t/i1}$  and the indole nitrogen restricts Trp 70 and drives the side chain into contact with  $\alpha_{t/i1}$  residues Arg 204 and Trp 207 (Fig. 3e). In exchange, Trp 254 of  $\alpha_{t/i1}$  extends towards the PDE $\gamma$   $\alpha 3$  helix, forming hydrophobic and polar interactions with five PDE $\gamma$  residues. In contrast to the RGS9/ $\alpha_{t/i1}$  interface discussed below, the PDE $\gamma$ / $\alpha_{t/i1}$  interface is nearly devoid of solvent (Fig. 3b).

The heterotrimeric structure confirms the switch II/ $\alpha 3$  cleft as a primary determinant in PDE $\gamma$  binding<sup>4,14</sup>. Alanine scanning mutagenesis of  $\alpha_t$ , coupled with binding and GTPase assays, implicated Arg 201, Arg 204, Trp 207, Ile 208 of switch II and His 244 of  $\alpha 3$  as residues that bind PDE $\gamma$ <sup>15</sup>. The structure is also in accord with an  $\alpha_t$  mutation that disrupts the switch II/ $\alpha 3$  cleft, prevents PDE $\gamma$  binding and underlies the molecular basis for Nougaret night blindness<sup>16</sup>. The structure is not consistent with crosslinking results<sup>17,18</sup> implicating binding regions outside the switch II/ $\alpha 3$  cleft.

The  $\alpha_{t/i1}$ /PDE $\gamma$  interaction reveals an emerging paradigm in heterotrimeric G-protein/effector coupling. Temporally regulated effector activation requires a GTP-dependent  $G\alpha$ -binding site, restricting effector binding to  $G\alpha$  sites that are switch region inclusive. In addition, the binding site must confer effector specificity. Switch II and  $\alpha 3$ , together, meet both requirements without compromising the RGS-binding site (Fig. 3f). PDE $\gamma$  binding involves a number of key residues in the  $\alpha_{t/i1}$  switch II/ $\alpha 3$  cleft: Arg 204, Trp 207, Phe 211, Leu 245 and Trp 254 (Fig. 5a).

The structure of adenylyl cyclase VC<sub>1</sub>IIC<sub>2</sub> in complex with  $\alpha_s$ -GTP $\gamma$ S<sup>19</sup> reveals a strong similarity in effector binding (Fig. 5b). In PDE $\gamma$  binding, Trp 254 of  $\alpha_t$  makes hydrophobic contacts with

Leu 78 and Leu 81 of PDE $\gamma$ , and forms a hydrogen bond between its indole nitrogen and the Leu 76 backbone. In adenylyl cyclase binding, the corresponding  $\alpha_s$  residue, Trp 281, makes concerted hydrophobic contacts with Phe 379 of VC<sub>1</sub> and His 989 of IIC<sub>2</sub>. A hydrogen bond from Glu 917 to the indole nitrogen of Trp 281 directly parallels the interaction of Leu 76 of PDE $\gamma$  with Trp 254. Analogous to the key PDE $\gamma$  residue Trp 70, the adenylyl cyclase IIC<sub>2</sub> residue Phe 991 is inserted into the switch II/ $\alpha 3$  cleft forming homologous hydrophobic contacts with residues Arg 231, Trp 234, Phe 238 and Leu 272 of  $\alpha_s$ . Similar to the effects of the PDE $\gamma$  mutation Trp70Ala, the IIC<sub>2</sub> mutation, Phe991Ala, results in decreased  $\alpha_s$ -mediated stimulation of adenylyl cyclase activity<sup>20</sup>. It is likely that the  $G\alpha$  switch II/ $\alpha 3$  cleft is involved in interactions with other effector molecules, particularly where effector activation is found coupled with RGS activity.

By sequestering PDE $\gamma$  residues implicated in PDE $\alpha\beta$  inhibition, the  $\alpha_{t/i1}$ -GDP- $AlF_4^-$ -PDE $\gamma$ -RGS9 structure reveals the mechanism of PDE activation. Proteolysis experiments<sup>21</sup> and deletion mutagenesis<sup>22</sup> have localized the inhibitory region of PDE $\gamma$  to the C-terminal five amino acids. Ile 87, the C-terminal residue of PDE $\gamma$ , forms contacts with switch II residues Ile 208, His 209 and Lys 212. As a result, the PDE $\gamma$  C-terminal region is pulled towards switch II (Fig. 1) and is partially shielded by Phe 50 of PDE $\gamma$  (Fig. 3f). These interactions constrain the PDE $\gamma$  C terminus and prevent access to PDE $\alpha\beta$ . In this state, PDE $\alpha\beta$  proceeds with the catalysis of cGMP, propagating and amplifying the visual signal until GTP hydrolysis inactivates  $\alpha_t$ , and the PDE $\gamma$  C terminus returns to its inhibitory site on PDE $\alpha\beta$ .



**Figure 2** Sequence alignment and secondary-structure features of RGS domains, PDE $\gamma$  subunits and  $G\alpha$  subunits. Secondary-structure elements from the  $\alpha_{t/i1}$ -GDP- $AlF_4^-$ -PDE $\gamma$ -RGS9 complex are indicated above the alignments by rectangles ( $\alpha$ -helices) and arrows ( $\beta$ -strands). Residue numbers are shown for RGS9, rod PDE $\gamma$  and  $\alpha_{t/i1}$ . Residues involved in more than one of the above interactions have coloured blocks

below the alignment indicative of the additional interaction(s). Specific interactions are less than 4 Å apart. GenBank accession numbers for proteins from top to bottom are 046469, P97428, P49799, NP\_005864, P49809, P11972, P04972, P22571, P04695, P04898, P04896, P08239.

Nucleotide hydrolysis produces a marked conformational change in switch II that distorts the  $\alpha_i$  effector site. The crystal structures of  $\alpha_t$ -GDP<sup>7</sup> and  $\alpha_{t/i1}$ -GDP- $\beta\gamma_t$  (ref. 23) show that, after GTP hydrolysis, switch II undergoes a torsional movement away from the  $\alpha_3$  helix. In the  $\alpha_{t/i1}$ -GDP- $\beta\gamma_t$  structure,  $\alpha_2$  is rotated  $\sim 90^\circ$  about its helical axis (Fig. 5c). The  $\alpha_{t/i1}$  residues Ser 248 and Arg 204, which are used in PDE $\gamma$  binding (Fig. 5a), now form an intimate interaction with one another (Fig. 5c). Trp 207 and Phe 211, previously exposed in the PDE $\gamma$ -binding site (Fig. 5a), are now positioned on the opposite side of switch II and are used in a key set of hydrophobic contacts with  $\beta_t$  residues Trp 99, Leu 117 and Tyr 145 (Fig. 5c). In effect, nucleotide hydrolysis and G $\alpha\beta\gamma$  heterotrimer formation abrogates the G $\alpha$ -binding site used for PDE $\gamma$  and adenylyl cyclase interactions.

Although our construct, PDE $\gamma_{46-87}$ , contains the regions involved in nucleotide-dependent binding to  $\alpha_t$ , GAP potentiation and PDE $\alpha\beta$  inhibition, a central polycationic region not present in our construct has been implicated in nucleotide-independent binding to  $\alpha_t$ . The proposed binding site for the polycationic region is the  $\alpha_t$   $\alpha_3$ - $\beta_5$  region<sup>4</sup>. A likely trajectory from the first residue modelled (PDE $\gamma$  Phe 50) to the  $\alpha_3$ - $\beta_5$  zone would bring the PDE $\gamma$  N-terminal region through a groove created by the RGS9  $\alpha_3/\alpha_4$  loop and the  $\alpha_3$ /C-terminal region of PDE $\gamma$ . This route would further restrain the PDE $\gamma$  C terminus and augment the PDE $\gamma$ /RGS9 interface.

PDE $\gamma$  inactivates transducin by potentiating RGS9 GAP activity<sup>2,5</sup>. The heterotrimeric structure reveals four possible means that PDE $\gamma$  uses to enhance RGS9 activity. First, PDE $\gamma$  expands the switch II/ $\alpha_3$  cleft and positions switch II in the

transition state conformation most favoured for RGS9 binding. Switch II residues involved in PDE $\gamma$  interactions dovetail with switch II residues involved in RGS9 interactions (Fig. 2). As a result, switch II is utilized to bind PDE $\gamma$  and RGS9 cooperatively.

Second, PDE $\gamma$  perturbs key transducin residues involved in RGS9 binding and GTP hydrolysis. PDE $\gamma$  constrains  $\alpha_{t/i1}$  Arg 204 through contacts with PDE $\gamma$  Ile 67, Pro 69 and Trp 70 (Fig. 3e). As observed in the  $\alpha_t$ -GTP $\gamma$ S structure, Arg 204 forms two key hydrogen bonds: one from the N $\epsilon$  nitrogen to the Gly 199 carbonyl and a second  $\alpha$ -helical hydrogen bond from the Arg 204 peptide amide nitrogen to the Gln 200 backbone carbonyl. Thus, Arg 204 effectively positions the backbone of transducin Gln 200, a key residue for GTP hydrolysis and the RGS9 GAP mechanism (discussed below). The PDE $\gamma$ -mediated perturbation of the Gln 200 backbone orients the side chain for optimal interaction with the RGS9 residue Asn 364. In addition, repositioning the Gln 200 backbone may facilitate the release of the nucleophilic water which, in the  $\alpha_t$ -GTP $\gamma$ S structure, is bound to the Gln 200 backbone amide nitrogen<sup>6</sup>.

The third PDE $\gamma$  interaction mediates stabilization of the hydrolytic intermediate (Fig. 3e). Trp 70 of PDE $\gamma$  conformationally restricts Trp 207 of  $\alpha_{t/i1}$ , stabilizing the hydrogen bond that Trp 207 forms between its indole nitrogen and the Gly 198 carbonyl. This constraint on the Gly 198/Gly 199 peptide bond orients the backbone amide nitrogen in a conformation that stabilizes the hydrolytic intermediate. Thus, PDE $\gamma$  and RGS9 cooperate in stabilizing the transition state.

Last, a small RGS9/PDE $\gamma$  interface increases the available RGS9-binding site. A hydrophobic interaction between Trp 362 of RGS9 and Val 66 of PDE $\gamma$  (Fig. 3a), coupled with local electrostatic charge

**Table 1 Crystallographic data, phasing and refinement**

<b>RGS9</b>						
Space group: C2	Cell dimensions: $a = 67.3 \text{ \AA}$ , $b = 71.8 \text{ \AA}$ , $c = 34.6 \text{ \AA}$ , $\alpha = 90^\circ$ , $\beta = 96.1^\circ$ , $\gamma = 90^\circ$				Phasing power†	
Data Statistics:	$d_{\min}$ (Å)	Completeness (%)	$I/\sigma$	$R_{\text{sym}}(\%)*$	+ Friedel mate	- Friedel mate
Se-Met $\lambda_1$ (1.0283 Å)	2.13	97.1 (91.8)	29.2 (10.3)	4.0 (11.3)	0.87 (0.62)	1.10 (0.77)
Se-Met $\lambda_2$ (0.9795 Å)	2.04	98.0 (97.3)	27.1 (8.4)	4.2 (13.7)	1.11 (0.62)	3.14 (1.71)
Se-Met $\lambda_3$ (0.9793 Å)	2.04	98.0 (98.2)	16.4 (16.1)	5.2 (11.1)	1.14 (0.97)	2.22 (1.61)
Se-Met $\lambda_4$ (0.9351 Å)	1.94	97.7 (91.9)	23.5 (3.1)	5.1 (30.1)	Reference	1.93 (0.87)
Refinement	(50 - 1.94 Å)					
$R$ value‡	22.1 (25.6)					
$R_{\text{free}}§$	24.8 (27.0)					
Mean $B$ factor (min/max)	28.7 Å <sup>2</sup> (13.1 Å <sup>2</sup> /58.5 Å <sup>2</sup> )					
<b><math>\alpha_{t/i1}</math>-GDP-AIF<sub>4</sub>-RGS9</b>						
Space group: P2 <sub>1</sub> 2 <sub>1</sub> 2 <sub>1</sub>	Cell dimensions: $a = 96.8 \text{ \AA}$ , $b = 115.1 \text{ \AA}$ , $c = 136.5 \text{ \AA}$ , $\alpha = 90^\circ$ , $\beta = 90^\circ$ , $\gamma = 90^\circ$				Phasing power†	
Data statistics:	$d_{\min}$ (Å)	Completeness (%)	$I/\sigma$	$R_{\text{sym}}(\%)*$	+ Friedel mate	- Friedel mate
Native (1.0281 Å)	2.30	96.9 (79.6)	28.5 (1.6)	6.0 (52.7)		
Se-Met $\lambda_1$ (1.0281 Å)	2.60	88.9 (43.9)	16.6 (1.5)	6.8 (49.5)	0.85 (0.54)	0.94 (0.56)
Se-Met $\lambda_2$ (0.9794 Å)	2.60	92.1 (54.9)	16.3 (1.5)	7.4 (47.9)	1.41 (0.49)	2.09 (0.63)
Se-Met $\lambda_3$ (0.9792 Å)	2.65	93.4 (62.7)	15.8 (1.6)	8.0 (48.5)	0.91 (0.59)	1.74 (0.65)
Se-Met $\lambda_4$ (0.9349 Å)	>2.80	97.9 (84.8)	16.3 (1.9)	8.2 (51.6)	Reference	1.00 (0.38)
Refinement	(50 - 2.30 Å)					
$R$ value‡	23.1 (38.6)					
$R_{\text{free}}§$	26.8 (40.3)					
Mean $B$ factor (min/max)	65.7 Å <sup>2</sup> (32.5 Å <sup>2</sup> /127.5 Å <sup>2</sup> )					
<b><math>\alpha_{t/i1}</math>-GDP-AIF<sub>4</sub>-PDE<math>\gamma</math>-RGS9</b>						
Space group: P2 <sub>1</sub> 2 <sub>1</sub> 2 <sub>1</sub>	Cell dimensions: $a = 91.6 \text{ \AA}$ , $b = 115.9 \text{ \AA}$ , $c = 134.2 \text{ \AA}$ , $\alpha = 90^\circ$ , $\beta = 90^\circ$ , $\gamma = 90^\circ$				Phasing power†	
Data statistics:	$d_{\min}$ (Å)	Completeness (%)	$I/\sigma$	$R_{\text{sym}}(\%)*$	+ Friedel mate	- Friedel mate
Native (0.9793 Å)	2.02	99.8 (99.7)	19.5 (4.4)	9.0 (55.3)		
Se-Met $\lambda_1$ (1.0280 Å)	2.40	99.2 (94.6)	13.7 (2.1)	9.0 (49.3)	0.80 (0.62)	0.91 (0.69)
Se-Met $\lambda_2$ (0.9794 Å)	2.40	99.5 (96.9)	13.3 (1.8)	9.7 (51.9)	1.28 (0.74)	1.69 (0.84)
Se-Met $\lambda_3$ (0.9792 Å)	2.40	99.3 (95.8)	13.6 (1.9)	9.7 (50.5)	0.91 (0.69)	1.56 (0.84)
Se-Met $\lambda_4$ (0.9349 Å)	2.60	99.7 (98.3)	11.6 (2.4)	11.5 (53.1)	Reference	0.86 (0.56)
Refinement	(50 - 2.02 Å)					
$R$ value‡	23.3 (31.9)					
$R_{\text{free}}§$	26.5 (35.1)					
Mean $B$ factor (min/max)	33.8 Å <sup>2</sup> (6.2 Å <sup>2</sup> /103.5 Å <sup>2</sup> )					

Values in parentheses are for the highest resolution shells. All data sets had an average redundancy of 3.1 or higher.

\*  $R_{\text{sym}} = \sum_i \sum_j |I_i(h) - I_j(h)| / \sum_i \sum_j I_i(h)$  where  $I_i(h)$  is the integrated intensity of the  $i$ th reflection with the Miller index  $h$  and  $I_j(h)$  is the average over Friedel and symmetry equivalents.

† MAD phasing power is defined as  $(|F_D - F_N|^2) / (|F_D|^2 + |F_N|^2)$  where  $F_D$  is the experimental phase probability distribution,  $F_N$  are structure factors at the reference wavelength  $\lambda_r$ , and  $F_D$  are structure factors of + or - Friedel mates at the other designated wavelength.  $\Delta F_N$  is the difference in heavy atom structure factors between two wavelengths.

‡  $R$  value =  $\sum(|F_{\text{obs}}| - k|F_{\text{calc}}|) / \sum|F_{\text{obs}}|$ .

§  $R_{\text{free}}$  is calculated using a 10% subset of the data which was removed randomly from the original data and excluded from refinement.

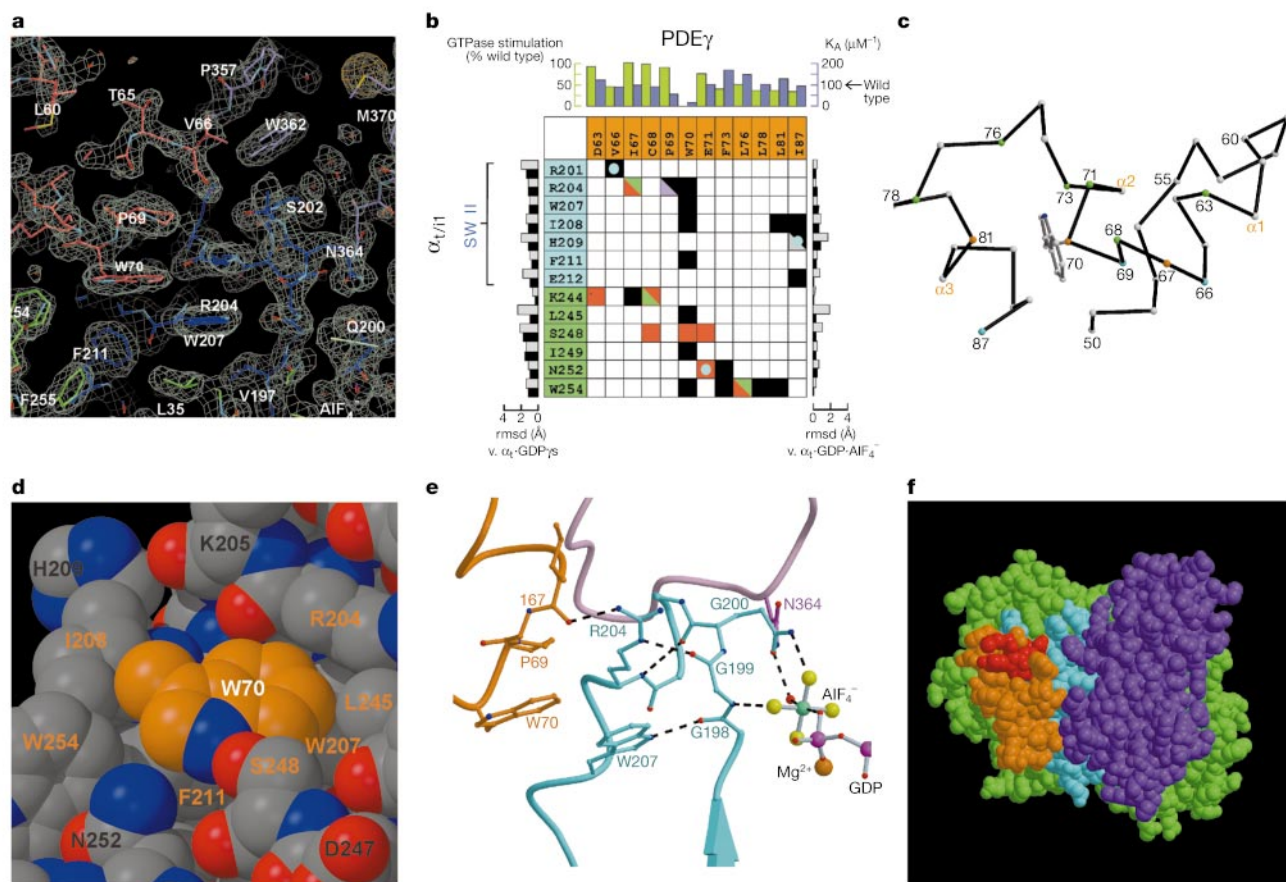


**Figure 3** PDE $\gamma$ / $\alpha_{I/1}$  interactions. **a**,  $\sigma_A$ -weighted  $2F_o - F_c$  electron density map for  $\alpha_{I/1}$ -GDP·AlF $_4^-$ ·PDE $\gamma$ -RGS9 (1.5 $\sigma$ ). Anomalous difference Fourier density (15 $\sigma$ ) in coral. **b**, Intermolecular contact (sub 4 Å) matrix for PDE $\gamma$  residues (orange) that contact  $\alpha_{I/1}$  non-switch residues (green) or  $\alpha_{I/1}$  switch residues (blue). Electrostatic interactions to side chains are shown in red, to main chain in green. van der Waals contacts to side chains, to main chain or to both are shown in black, grey and lavender, respectively. Water-mediated interactions are indicated by blue circles. The root-mean-square deviation (rmsd) for  $\alpha_{I/1}$  contact residues (C $\alpha$  atoms are in black, overall side-chain

deviation in grey) is shown for  $\alpha_{I/1}$ -RGS9 versus  $\alpha_I$ -GTP $\gamma$ S (left)<sup>6</sup> and  $\alpha_I$ -GDP·AlF $_4^-$  (right)<sup>8</sup>. Results of PDE $\gamma$  alanine scanning mutagenesis on GTPase stimulation (light-green bars) and  $K_A$  (dark-blue bars; ref. 13) are shown above. **c**, C $\alpha$  trace of PDE $\gamma_{50-87}$ . C $\alpha$  atoms of residues contacting  $\alpha_{I/1}$  switch II, the  $\alpha_3/\alpha_3$ - $\beta_5$  loop region or both are in blue, green and orange, respectively. **d**, CPK representation of PDE $\gamma$  W70 in the switch II/ $\alpha_3$  groove with residues that contact W70 in orange. **e**, Diagram of PDE $\gamma$ /switch II/RGS9 interactions coloured as in **a**. **f**, CPK representation of the heterotrimeric complex with the five C-terminal amino acids of PDE $\gamma$  in red.

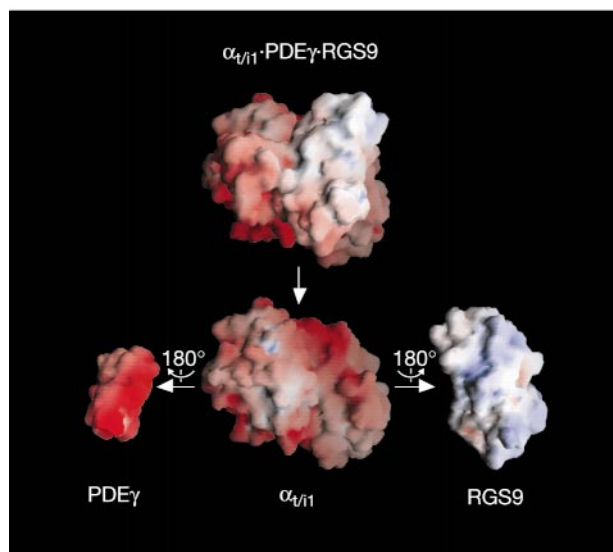


**Figure 4** Solvent-accessible surface coloured according to electrostatic potential in the range  $-10k_B T$  (red) to  $+10k_B T$  (blue), where  $k_B$  is Boltzmann's constant, and  $T$  is the absolute temperature (in K). The trimeric complex is shown above in the same orientation

as in Fig. 3f. The orientation is maintained below except that PDE $\gamma$  and RGS9 are translated horizontally and rotated 180° about the vertical axis.

complementation, supplements the RGS9-binding site by burying an additional  $\sim 200 \text{ \AA}^2$  of solvent-accessible surface. The proximity of the PDE $\gamma$ /RGS9 interface to the critical RGS9 GAP residue Asn 364 is likely to support GAP activity.

The RGS9/ $\alpha_{t/i1}$  interface is highly solvated and is dominated by interactions from the RGS9  $\alpha 3/\alpha 4$ ,  $\alpha 5/\alpha 6$  and  $\alpha 7/\alpha 8$  loops to the  $\alpha_{t/i1}$  switch regions I and II (Fig. 6a) which buries  $1,800 \text{ \AA}^2$  of solvent-accessible surface. The catalytic face of RGS9 is predominantly positively charged and complements the negatively charged  $\alpha_{t/i1}$  binding surface (Fig. 4). A comparison of the interactions within the RGS4- $\alpha_{i1}$  complex<sup>9</sup> with those within the RGS9- $\alpha_{t/i1}$  complex reveals minor deviations. The RGS9- $\alpha_{t/i1}$  complex contains fewer switch III interactions, and fewer total interactions. Analysis of all RGS9- $\alpha_{t/i1}$  protomers solved reveals a plasticity in the binding interface possibly indicative of the RGS protein's ability to recognize a range of switch conformations during GTP hydrolysis.

Comparison of the RGS9  $\alpha_{t/i1}$  structure with its independently solved component parts reveals structural changes that occur on complex formation. On binding, RGS9 causes switches I and II to move closer to each other, and induces an interswitch stabilization

that is absent in the  $\alpha_t$ -GDP- $\text{AlF}_4^-$  structure. RGS9 residue Asn 325 causes the side chain of Thr 178 in switch I to rotate  $\sim 120^\circ$ , forming interactions between Thr 178 of switch I and residues Lys 206 and Glu 203 of switch II (Fig. 6e). Thus, RGS9 binds  $\alpha_{t/i1}$ , serving as an external scaffold for the transition state architecture while simultaneously inducing internal switch region stabilization.

RGS9 undergoes moderate conformational changes on binding  $\alpha_{t/i1}$ . The  $\alpha 5/6$  loop exhibits the greatest change, repositioning the critical GAP residue Asn 364 (Fig. 6b). In the RGS9 structure, Asn 364 forms hydrophobic interactions with Trp 362 (Fig. 6c). On binding  $\alpha_{t/i1}$ , the Asn 364/Trp 362 interaction is disrupted by the insertion of Ser 202 of  $\alpha_{t/i1}$  (Fig. 6d). Serine 202 is conserved among  $\alpha_i$  family members, but the corresponding residue in  $\alpha_s$  is an aspartic acid. The  $\alpha_{t/i1}$  mutation Ser202Asp prevents the RGS interaction and explains the immunity of  $\alpha_s$  to RGS GAP activity<sup>24</sup>. A second critical residue for the RGS GAP mechanism is Asp 399, which is partially disordered in the RGS9 structure. On binding  $\alpha_{t/i1}$ , Asp 399 interacts with RGS9 residues Arg 403 and Glu 320 and is positioned for switch I stabilization (Fig. 6e).

A number of RGS proteins exhibit GAP activity on  $\alpha_t$  *in vitro*, but the specificity of RGS9 lies in its PDE $\gamma$ -mediated potentiation. The effect of PDE $\gamma$  on other RGS proteins is GAP suppression<sup>25</sup>. The RGS9 region involved in PDE $\gamma$  specificity has been localized to the  $\alpha 5/6$  loop<sup>26,27</sup>. This loop region interacts with both switch II and PDE $\gamma$  through a unique complementation of electrostatic (RGS9 Arg 360/PDE $\gamma$  Asp 52) and hydrophobic (RGS9 Trp 362/PDE $\gamma$  Val 66) interactions. The RGS9 residues used in this region are unique to RGS9. In most RGS proteins, Arg 360 and Trp 362 are replaced by proline and glutamate, respectively. The repulsive effects of altering the electrostatic and hydrophobic nature of the  $\alpha 5/6$  loop would inevitably force the proximal Asn 364 out of position. As discussed below, Asn 364 is a key component of the GAP mechanism; disrupting its position would have deleterious effects on GAP activity.

RGS9 increases the GTP hydrolysis rate by stabilization of the  $\alpha_{t/i1}$  switch regions in their transition state conformation and orientation of the critical  $\alpha_{t/i1}$  carbonyls used to position the nucleophilic water as previously suggested<sup>9</sup>. At switch I, interactions of RGS9 residues Asn 325 and Asp 399 with  $\alpha_{t/i1}$  Thr 178 effectively position the adjacent  $\alpha_{t/i1}$  Thr 177 backbone carbonyl for stabilization of the nucleophilic water (Fig. 6e). The imposed constraints position Thr 178 and the switch I backbone in a different orientation from that observed in the  $\alpha_t$ -GDP- $\text{AlF}_4^-$  structure (Fig. 6a).

At switch II, the orientation of RGS9 Asn 364 is dictated by hydrogen bonds to  $\alpha_{t/i1}$  residues Lys 176 and Glu 203 (Fig. 6e). As positioned, the Asn 364 side-chain amide nitrogen resolves the torsional ambiguity of  $\alpha_{t/i1}$  Gln 200. As a result, the Gln 200 side-chain carbonyl is positioned to stabilize the nucleophilic water while the Gln 200 side-chain nitrogen is positioned to stabilize the  $\gamma$ -phosphate planar intermediate.

The heterotrimeric structure reveals details of the catalytic site at 2.0  $\text{\AA}$  resolution, allowing the unambiguous conclusion that RGS proteins do not directly contribute to the active site by donating residues or through water-mediated interactions.

The  $\alpha_{t/i1}$ -GDP- $\text{AlF}_4^-$ -PDE $\gamma$ -RGS9 structure reveals several important features of the mammalian rod visual cascade that facilitate signal transmission, amplification and sub-second recovery. Effector/GAP coupling is likely to be found in other high-fidelity signalling systems where a G protein must remain active until it reaches its effector target, at which point it is inactivated, ensuring signal efficiency.  $\square$

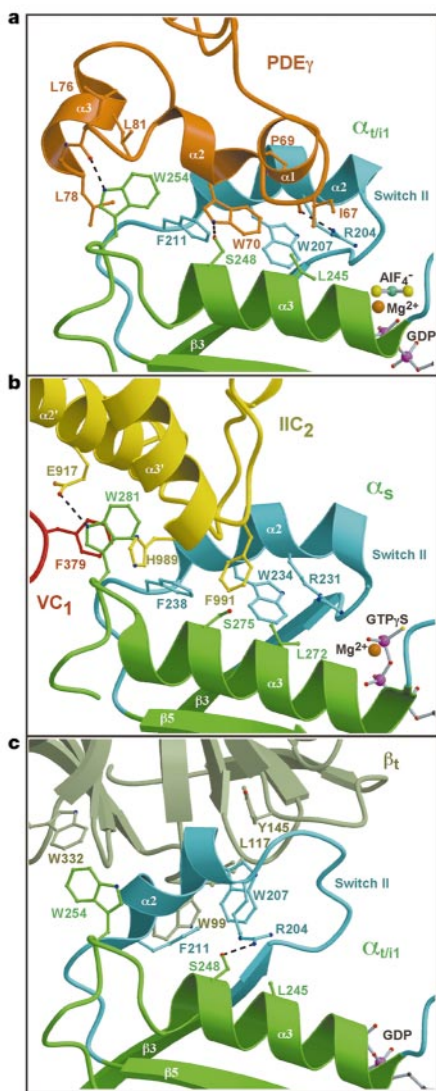


**Figure 5** Interaction modes of the  $G\alpha$  switch II region with  $G\alpha$  effector molecules and the  $G\beta\gamma$  subunit. **a**, Interaction of PDE $\gamma$  with  $\alpha_{t/i1}$ -GDP- $\text{AlF}_4^-$ . The colouring scheme is the same as in Fig. 1. **b**, Interaction of adenylyl cyclase constructs VC<sub>1</sub> (red) and IIC<sub>2</sub> (yellow) with  $\alpha_s$ -GTP- $\gamma$ S<sup>19</sup>. The  $\alpha_s$  colouring scheme is homologous to that used for  $\alpha_{t/i1}$  in **a**. **c**, Interaction of  $\beta_t$  (grey-green) with  $\alpha_{t/i1}$ -GDP (coloured as in **a**)<sup>23</sup>.

## Methods

### Protein expression, purification and crystallization

We subcloned bovine complementary DNA encoding the RGS9 RGS domain<sup>2</sup> (residues 276–422) into pGEX-2T (Pharmacia). Native and Se-Met-substituted RGS9 proteins were expressed in *Escherichia coli* and purified using glutathione Sepharose 4B (Pharmacia).

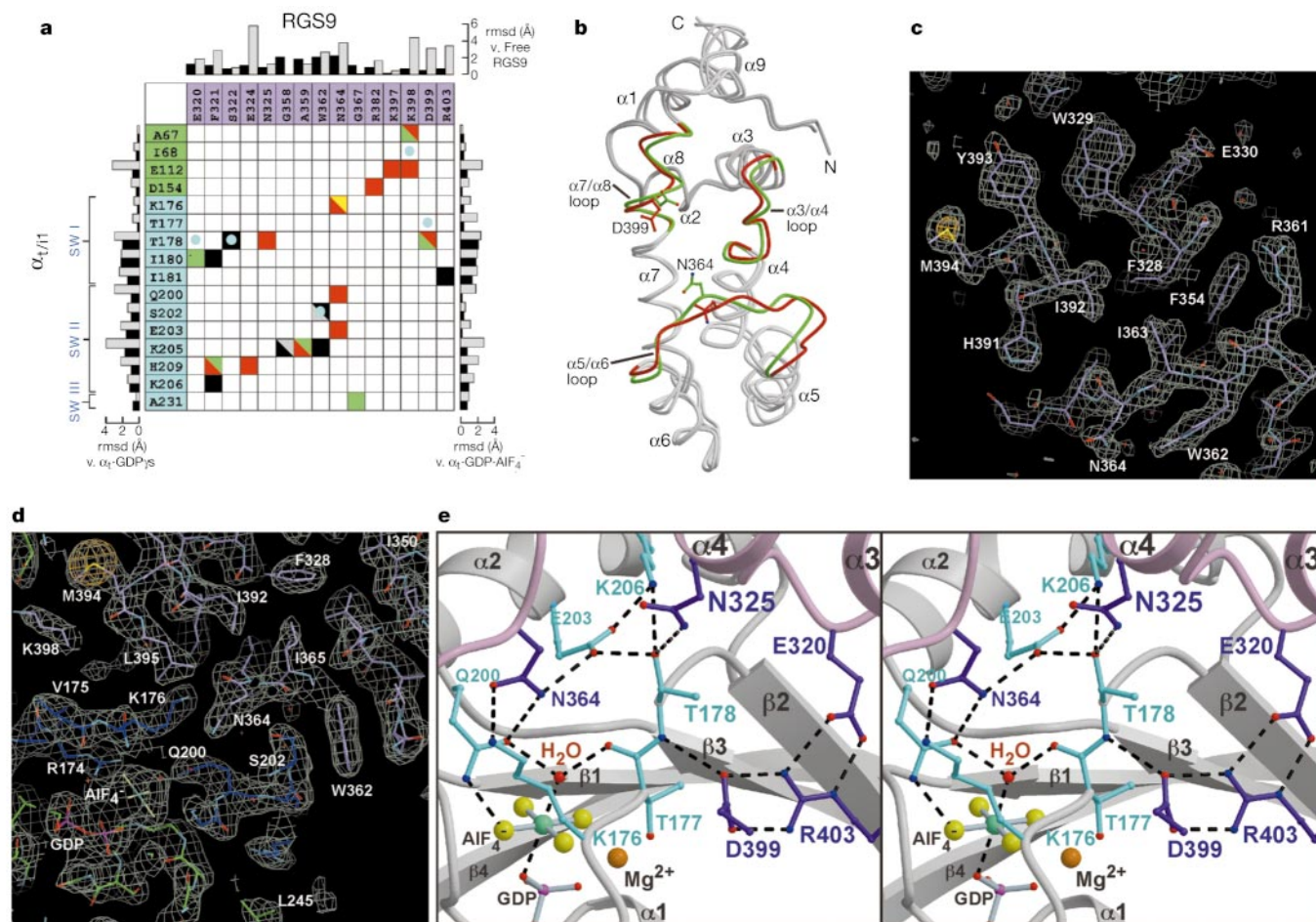


**Figure 6** RGS9/ $\alpha_{11}$  interactions. **a**, Intermolecular contact matrix for RGS9 residues (lavender) that contact  $\alpha_{11}$  residues represented as in Fig. 3b except that yellow indicates electrostatic interactions to both side-chain and main-chain atoms. **b**, C $\alpha$  trace comparison of RGS9 interaction loops: RGS9 alone (red) compared with RGS9 in complex

with  $\alpha_{11}$  (green). **c**, **d**,  $\alpha$ A-weighted  $2F_o - F_c$  electron density map ( $1.5\sigma$ ) and anomalous difference Fourier density ( $15\sigma$ , in coral) of RGS9 (**c**) and  $\alpha_{11}$ -GDP- $\text{AlF}_4^-$ -RGS9 (**d**). **e**, Stereo-pair ball-and-stick model of the active site. RGS9 and  $\alpha_{11}$  are pink and grey, respectively.

Fusion protein was cleaved with thrombin and subjected to cation exchange chromatography.  $\alpha_{11}$  was prepared as described<sup>4</sup>, except that  $\alpha_{11}$ -GDP- $\text{AlF}_4^-$  was treated with endoproteinase LysC to produce residues 26–350 of  $\alpha_{11}$ . We subcloned DNA encoding the bovine PDE $\gamma$  subunit (GenBank accession number M28853) (residues 46–87) into pGEX-2T, expressed it in *E. coli*, and purified it using glutathione Sepharose 4B. Fusion protein was cleaved with thrombin and subjected to Q Sepharose and Superdex 75 16/60 (Pharmacia) chromatography.

The  $\alpha_{11}$ -GDP- $\text{AlF}_4^-$ -RGS9 complex was formed and purified using a described protocol<sup>9</sup>. All crystals were obtained by hanging-drop vapour diffusion at 4 °C against 1 ml of respective mother liquor. A Se-Met RGS9 crystal was obtained by mixing 1.5  $\mu\text{l}$  of RGS9 at 15 mg ml<sup>-1</sup> with 1.5  $\mu\text{l}$  mother liquor (15.5% PEG 8000, 50 mM Tris pH 8.0, 5% ethylene glycol, 75 mM NaCl). The crystal was transferred to 12% PEG 8000, 50 mM Tris pH 8.0, 25% ethylene glycol, 75 mM NaCl and flash frozen. The crystal belongs to the space group C2 with one molecule per asymmetric unit.  $\alpha_{11}$ -GDP- $\text{AlF}_4^-$ -RGS9 crystals (native and RGS9<sub>Se-Met</sub> substituted) were obtained by mixing 1.5  $\mu\text{l}$  of  $\alpha_{11}$ -GDP- $\text{AlF}_4^-$ -RGS9 at 20 mg ml<sup>-1</sup> with 1.5  $\mu\text{l}$  of mother liquor (10.5% PEG 8000, 110 mM magnesium acetate, 50 mM Tris pH 8.5, 0.2%  $\beta$ -mercaptoethanol). Crystals were transferred into mother liquor plus 35% glycerol and flash frozen. Crystals belong to the space group P2<sub>1</sub>2<sub>1</sub>2<sub>1</sub> with two complexes per asymmetric unit. The  $\alpha_{11}$ -GDP- $\text{AlF}_4^-$ -PDE $\gamma$ -RGS9 complex was formed by incubating a 1:1 molar ratio of PDE $\gamma$  and  $\alpha_{11}$ -GDP- $\text{AlF}_4^-$ -RGS9 at 4 °C for 1 h. Heterotrimer crystals (native and RGS9<sub>Se-Met</sub> derivatized) were obtained by mixing 1.5  $\mu\text{l}$  of  $\alpha_{11}$ -GDP- $\text{AlF}_4^-$ -PDE $\gamma$ -RGS9 at 20 mg ml<sup>-1</sup> with 1.5  $\mu\text{l}$  mother liquor (15.0% PEG 8000, 200 mM Tris pH 9.0, 0.2%  $\beta$ -mercaptoethanol, 1 mM (NH<sub>4</sub>)<sub>2</sub>WS<sub>4</sub>). The cryopreservation protocol is analogous to that used for the heterodimer crystals. Crystals belong to the space group P2<sub>1</sub>2<sub>1</sub>2<sub>1</sub> and contain one  $\alpha_{11}$ -GDP- $\text{AlF}_4^-$ -PDE $\gamma$ -RGS9 complex and one  $\alpha_{11}$ -GDP- $\text{AlF}_4^-$ -RGS9 complex per asymmetric unit.

**Data collection, structure solution and refinement**

Diffraction data were measured at the Argonne National Laboratory (ANL) Advanced Photon Source (APS) Structural Biology Center (SBC) 19-ID beamline, and processed and scaled using HKL2000 (ref. 28). Selenium MAD data were collected using inverse beam

geometry. Heavy-atom searches and phasing were performed using the CNS package<sup>29</sup>. Selenium sites were found by using an automated Patterson heavy atom search method and peak anomalous wavelength data. MAD phasing used selenium coordinates and the high energy remote wavelength as reference. Phases were improved by solvent flipping and histogram matching, and where applicable, extended to the resolution of the native data set. Model building was done with O<sup>30</sup>. Refinement was performed with the CNS package<sup>29</sup> and monitored with a random 10% of the data used for cross-validation. Model refinement employed the MLHL target function, torsion angle molecular dynamics simulated annealing, B-factor refinement, and rebuilding in O with  $\sigma_A$ -weighted difference Fourier maps. Three final rounds of refinement against an MLF target were performed for the  $\alpha_{11}$ -GDP- $\text{AlF}_4^-$ -RGS9 structure using native data. Figures were prepared with MOLSCRIPT, RASTER3D, O and GRASP.

Received 11 September; accepted 20 November 2000.

- Angleton, J. K. & Wensel, T. G. A GTPase-accelerating factor for transducin, distinct from its effector cGMP phosphodiesterase, in rod outer segment membranes. *Neuron* **11**, 939–949 (1993).
- He, W., Cowan, C. W. & Wensel, T. G. RGS9, a GTPase accelerator for phototransduction. *Neuron* **20**, 95–102 (1998).
- Chen, C.-K. *et al.* Slowed recovery of rod photoresponse in mice lacking the GTPase accelerating protein RGS9-1. *Nature* **403**, 557–560 (2000).
- Skiba, N. P., Bae, H. & Hamm, H. E. Mapping of effector binding sites of transducin  $\alpha$ -subunit using  $\text{G}\alpha/\text{G}\alpha_1$  chimeras. *J. Biol. Chem.* **271**, 413–424 (1996).
- Skiba, N. P., Yang, C.-S., Huang, T., Bae, H. & Hamm, H. E. The  $\alpha$ -helical domain of  $\text{G}\alpha$ , determines specific interaction with regulator of G protein signaling 9. *J. Biol. Chem.* **274**, 8770–8778 (1999).
- Noel, J. P., Hamm, H. E. & Sigler, P. B. The 2.2 Å crystal structure of transducin- $\alpha$  complexed with GTP $\gamma$ S. *Nature* **366**, 654–663 (1993).
- Lambright, D. G., Noel, J. P., Hamm, H. E. & Sigler, P. B. Structural determinants for activation of the  $\alpha$ -subunit of a heterotrimeric G protein. *Nature* **369**, 621–628 (1994).
- Sondek, J., Lambright, D. G., Noel, J. P., Hamm, H. E. & Sigler, P. B. GTPase mechanism of G proteins from the 1.7-Å crystal structure of transducin  $\alpha$ -GDP- $\text{AlF}_4^-$ . *Nature* **372**, 276–279 (1994).
- Tesmer, J. J. G., Berman, D. M., Gilman, A. G. & Sprang, S. R. Structure of RGS4 bound to  $\text{AlF}_4^-$ -activated  $\text{G}_{\text{in}\alpha}$ : Stabilization of the transition state for GTP hydrolysis. *Cell* **89**, 251–261 (1997).

10. Spink, K. E., Polakis, P. & Weis, W. I. Structural basis of the Axin–adenomatous polyposis coli interaction. *EMBO J.* **19**, 2270–2279 (2000).
11. De Alba, E., De Vries, L., Farquhar, M. G. & Tjandra, N. Solution structure of human GAIP (Gα interacting protein): a regulator of G protein signaling. *J. Mol. Biol.* **291**, 927–939 (1999).
12. Tsang, S. H. *et al.* Role for the target enzyme in deactivation of photoreceptor G protein *in vivo*. *Science* **282**, 117–121 (1998).
13. Slepak, V. Z. *et al.* An effector site that stimulates G-protein GTPase in photoreceptors. *J. Biol. Chem.* **270**, 14319–14324 (1995).
14. Faurobert, E., Otto-Bruc, A., Chardin, P. & Chabre, M. Tryptophan W207 in transducin Tα is the fluorescence sensor of the G protein activation switch and is involved in the effector binding. *EMBO J.* **12**, 4191–4198 (1993).
15. Natochin, M., Granovsky, A. E. & Artemyev, N. O. Identification of effector residues on photoreceptor G protein, transducin. *J. Biol. Chem.* **273**, 21808–21815 (1998).
16. Muradov, K. G. & Artemyev, N. O. Loss of the effector function in a transducin-α mutant associated with Nougaret night blindness. *J. Biol. Chem.* **275**, 6969–6974 (2000).
17. Liu, Y., Arshavsky, V. Y. & Ruoho, A. E. Interaction sites of the COOH-terminal region of the γ subunit of cGMP phosphodiesterase with the GTP-bound α subunit of transducin. *J. Biol. Chem.* **271**, 26900–26907 (1996).
18. Artemyev, N. O., Rarrick, H. M., Mills, J. S., Skiba, N. P. & Hamm, H. E. Sites of interaction between rod G-protein α-subunit and cGMP-phosphodiesterase γ-subunit: Implications for the phosphodiesterase activation mechanism. *J. Biol. Chem.* **267**, 25067–25072 (1992).
19. Tesmer, J. J. G., Sunahara, R. K., Gilman, A. G. & Sprang, S. R. Crystal structure of the catalytic domains of adenylyl cyclase in a complex with G<sub>o</sub>·GTPγS. *Science* **278**, 1907–1916 (1997).
20. Yan, S.-Z., Huang, Z.-H., Rao, V. D., Hurley, J. H. & Tang, W.-J. Three discrete regions of mammalian adenylyl cyclase form a site for G<sub>o</sub> activation. *J. Biol. Chem.* **272**, 18849–18854 (1997).
21. Lipkin, V. M., Dumler, I. L., Muradov, K. G., Artemyev, N. O. & Etingof, R. N. Active sites of the cyclic GMP phosphodiesterase γ-subunit of retinal rod outer segments. *FEBS Lett.* **234**, 287–290 (1988).
22. Brown, R. L. Functional regions of the inhibitory subunit of retinal rod cGMP phosphodiesterase identified by site-specific mutagenesis and fluorescence spectroscopy. *Biochemistry* **31**, 5918–5925 (1992).
23. Lambright, D. G. *et al.* The 2.0 Å crystal structure of a heterotrimeric G protein. *Nature* **379**, 311–319 (1996).
24. Natochin, M. & Artemyev, N. O. Substitution of transducin Ser<sup>202</sup> by Asp abolishes G-protein/RGS interaction. *J. Biol. Chem.* **273**, 4300–4303 (1998).
25. Nekrasova, E. R. *et al.* Activation of transducin guanosine triphosphatase by two proteins of the RGS family. *Biochemistry* **36**, 7638–7643 (1997).
26. McEntaffer, R. L., Natochin, M. & Artemyev, N. O. Modulation of transducin GTPase activity by chimeric RGS16 and RGS9 regulators of G protein signaling and the effector molecule. *Biochemistry* **38**, 4931–4937 (1999).
27. Sowa, M. E., He, W., Wensel, T. G. & Lichtarge, O. A regulator of G protein signaling interaction surface linked to effector specificity. *Proc. Natl Acad. Sci. USA* **97**, 1483–1488 (2000).
28. Otwinowski, Z. & Minor, W. Processing of X-ray diffraction data collected in oscillation mode. *Methods Enzymol.* **276**, 307–326 (1997).
29. Brunger, A. T. *et al.* Crystallography & NMR system: A new software suite for macromolecular structure determination. *Acta Crystallogr. D* **54**, 905–921 (1998).
30. Jones, T. A., Zou, J. Y., Cowan, S. W. & Kjeldgaard, M. Improved methods for building protein models in electron-density maps and the location of errors in these models. *Acta Crystallogr. A* **47**, 110–119 (1991).

**Acknowledgements**

We thank C. Berlot, Y. Korkhin, D. Lambright, L. Rice and J. Steitz for useful discussions; A. Brunger, P. Adams, R. Grosse-Kunstleve for help with CNS; and W. Minor and Z. Otwinowski for pre-release of HKL2000. We also thank staff of the SBC beamline 19-ID: R. Alkire, N. E.C. Duke, S. L. Ginell, K. Lazarski, S. Korolev, F. J. Rotella, R. Sanishvili, J. Lazarz, and A. Joachimiak. Use of the ANL SBC beamline at the APS was supported by the US Department of Energy, Office of Biological and Environmental Research. This work is supported in part by a NIH grant to P.B.S. M.A.K. is a HHMI Fellow of the LSRE. C.W.C. was supported by an NIH grant.

Correspondence and requests for materials should be addressed to K.C.S. (e-mail: kcs@mail.csb.yale.edu). Coordinates and structure factors are deposited in the Protein Data Bank under accession codes 1FQI, 1FQK and 1FQJ for RGS9, α<sub>i11</sub><sup>-</sup>·GDP·AlF<sub>4</sub><sup>-</sup>·RGS9, and α<sub>i11</sub><sup>-</sup>·GDP·AlF<sub>4</sub><sup>-</sup>·PDEγ·RGS9, respectively.